Volumetric Printing of Thiol-Ene Photo-Cross-Linkable Poly(ε-caprolactone): a Tunable Material Platform serving Biomedical Applications

*Quinten Thijssen, Astrid Quaak, Joseph Toombs, Elly De Vlieghere, Laurens Parmentier, Hayden Taylor, Sandra Van Vlierberghe**

Q. Thijssen, A. Quaak, Dr. E. De Vlieghere, L. Parmentier, Prof. Dr. S. Van Vlierberghe
Polymer Chemistry and Biomaterials Group, Centre of Macromolecular Chemistry, Department of Organic and Macromolecular Chemistry, Ghent University, Krijgslaan 281 S4, 9000, Belgium
E-mail: Sandra.VanVlierberghe@ugent.be

J. Toombs, Prof. Dr. H. Taylor
Department of Mechanical Engineering, University of California, Berkeley, 6159 Etcheverry Hall, Berkeley, CA 94720-1740

Keywords: poly(ε-caprolactone), thiol-ene, volumetric 3D-printing, computed axial lithography, tissue engineering

Current thoroughly described biodegradable and cross-linkable polymers mainly rely on acrylate cross-linking. However, despite the swift cross-linking kinetics of acrylates, the concomitant brittleness of the resulting materials limits their applicability. Here, we introduce photo-cross-linkable PCL networks through orthogonal thiol-ene chemistry. The step-growth polymerized networks are tunable, predictable by means of the rubber elasticity theory and it is shown that their mechanical properties are significantly improved over their acrylate cross-linked counterparts. Tunability is introduced to the materials, by altering M_c (or the molar mass

between cross-links), and its effect on the thermal properties, mechanical strength and degradability of the materials is evaluated. Moreover, excellent volumetric printability is illustrated and we report the smallest features obtained via volumetric 3D-printing to date, for thiol-ene systems. Finally, by means of *in-vitro* and *in-vivo* characterization of 3D-printed constructs, we illustrate that the volumetrically 3D-printed materials are biocompatible. This combination of mechanical stability, tunability, biocompatibility and rapid fabrication by volumetric 3D-printing charts a new path towards bedside manufacturing of biodegradable patient-specific implants.

1. Introduction

In an ideal world, damaged tissue would be restored back to its initial state, without the lingering presence of body foreign material, in a patient-specific manner. A generally accepted method by which this could be achieved is by means of a temporary scaffold.[1] This scaffold would temporarily take over the necessary functions of the defective tissue (for example, mechanical support). Over time, newly formed tissue would then replace the scaffold, re-take its function and restore the defective area to its initial state. This ideal scenario sets, among others, the following requirements for the temporary scaffold, irrespective of the targeted tissue type.

Firstly, the scaffold should be porous (to allow for tissue ingrowth), perfectly match the defective area (i.e., patient-specific implant or PSI) and be obtainable in a time-efficient manner.[2,3] To fulfill said requirements, volumetric 3D-printing (VP), also referred to as computed axial lithography (CAL), can be considered the ideal technique.[4] This approach, based on the sequential delivery of projections to a rotating resin, reduces the printing time to a range of tens of seconds, while maintaining µ-scale resolution.[5] To date, highly porous designs and (multi-)cm-scale objects have been printed by VP illustrating its suitability for the development of biodegradable implants.[4,5] Interestingly, the patient-specific design would be obtained through computed tomography (CT), and subsequently, the PSI would be 3D-printed via a process based on reversed-CT. In addition to the fast manufacturing speed, VP is distinct

from other (light-based) 3D-printing techniques as it enables overprinting of existing structures, obviates the need for supports and allows the use of viscous resins (> 4 Pa.s).[6–8]

Secondly, the scaffold should be mechanically stable and biodegradable, ideally in a tunable manner (in order to be matched to the respective tissue).[1,9] Based on these criteria, resorbable synthetic polymers such as poly(ε-caprolactone) (PCL) are promising given their degradability, mechanical properties and excellent biocompatibility.[10–15] While processing of resorbable synthetic polymers is unprecedented for VP to date, it has already been reported for conventional light/projection-based 3D-printing techniques (e.g., digital light processing).[16–21] However, to process PCL via light-mediated 3D-printing techniques, chemical functionalization of the PCL with photo-cross-linkable moieties is needed. In this context, functionalization with acrylates can be considered the gold standard. However, despite the swift cross-linking kinetics of acrylates, the concomitant brittleness of the resulting materials limits their applicability. Indeed, as opposed to their thermoplastic counterparts, that can be processed via extrusion-based 3D-printing, acrylate cross-linked PCL performs suboptimal from a mechanical perspective (ultimate strength < 2 MPa and elongation at break < 49%, *vide infra*).[16,22] To overcome this limitation, we have recently introduced thiol-ene cross-linking to photo-cross-link PCL which resulted in a ten-fold improvement of the ultimate strength and elongation at break as compared to the state-of-the-art.[23,24] This effect was attributed to the homogeneous network topology, stemming from the step-growth polymerization mechanism involved.[25]

In an attempt to progress towards the outlined ideal scenario, volumetric 3D-printing of tunable and mechanically robust thiol-ene cross-linked PCL networks is herein introduced. More precisely, alkene-functionalized PCL is synthesized in a controlled manner and cross-linked upon introduction of a tetra-functional thiol. To tune the physico-chemical properties of the designed networks, M_c (or the molar mass between cross-links) of the PCL precursors is varied. The effect of M_c on the physico-chemical properties is thoroughly elucidated as well as its effect

on the volumetric printability of the materials. Finally, the biocompatibility and toxicity of the volumetrically printed materials are evaluated.

This work establishes the novel thiol-ene cross-linked PCL networks as a biodegradable and tunable material platform serving volumetric 3D-printing. This combination of properties and rapid fabrication by VP charts a new path towards bedside manufacturing of PSI, while VP of (biodegradable) polyesters is unprecedented in the state-of-the-art.

2. Results and discussion

2.1. Synthesis and chemical characterization of alkene-functionalized PCL

In order to create thiol-ene cross-linked PCL networks with varying M_c (i.e., the molar mass between cross-links), different PCL precursors were first synthesized. More precisely, PCL precursors with an increasing number average molar mass (M_n) from 2300 to 4700, 6400 and 8700 $g.mol^{-1}$ were synthesized. To do so, the ring-opening polymerization (ROP) of ε-caprolactone was performed using tin octanoate as catalyst and glycol as initiator (Scheme 1). The molar mass of the precursors was controlled by manipulation of the monomer to initiator ratio. After overnight reaction, the monomer conversion exceeded 98% for all precursors.

To functionalize the precursors with telechelic alkene functionalities, the polymerization was followed by a post-polymerization modification (PPM) (Figure 1A). To this end, allyl isocyanate was introduced into the reaction mixture, leading to a swift conversion (i.e., quantitative conversion within 30 minutes of reaction time) of the terminal hydroxyl-functionalities (Scheme 1). Quantitative reaction was confirmed by the shift of the end-standing methylene moieties from 3.6 ppm to 3.8 ppm (Figure 1B). It should be noted that the synthesis and PPM were performed in one pot, without intermediate purification. Moreover, as tin octanoate also is an efficient catalyst for the urethane formation, no additional catalyst was needed for the PPM. The purified precursors were obtained after precipitation in diethyl ether with yields exceeding 90% (Table 1). In order to determine the degree of substitution (DS), quantitative ^{1}H-NMR spectroscopy (DMT as internal standard) was performed (Table S1-S2,

Figure S1-S2). The DS exceeded 99% for all PCL precursors (Table 1) and gel permeation chromatography (GPC) of the precursors further illustrated narrow polydispersities in the range of 1.12-1.21 (Figure 1C, Table 1). Finally, the chemical structure was further confirmed via FTIR spectroscopy (Figure S3).

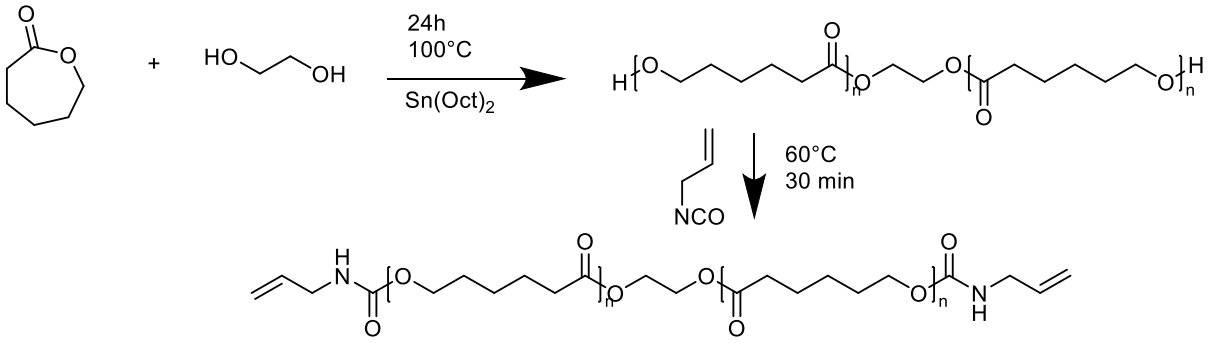

Scheme 1. Two-step, one-pot protocol for the synthesis of linear (bi-functional) alkene-functionalized PCL.

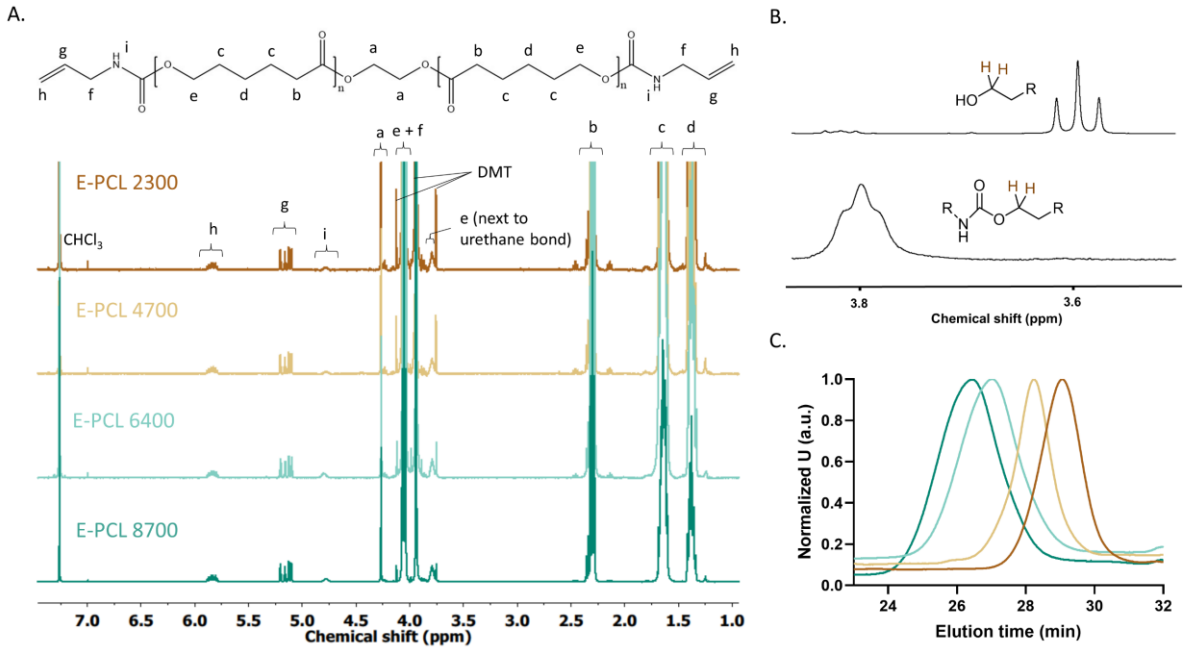

Figure 1. A. Assigned ^{1}H-NMR spectra of the various alkene-functionalized PCL precursors; B. ^{1}H-NMR spectrum illustrating quantitative conversion of the hydroxyl functionalities by shifted chemical shift of the terminal CH_2 moieties (3.6 to 3.8 ppm); C. Chromatograms obtained via GPC of the different PCL precursors.

Table 1. Overview of the synthesized PCL precursors with their respective alkene content, number average molar mass (M_n) determined via ^{1}H-NMR spectroscopy, degree of substitution (DS), conversion, yield and polydispersity (Đ). The corresponding color illustrated in the table is kept consistent throughout the article.

#	Color	'Ene' content (mmol.g^{-1}) [a]	M_n (^{1}H-NMR) (g.mol^{-1}) [a]	DS (%) [a]	Conversion (%)	Yield (%)	Đ
E-PCL 2300		0.89 ± 0.01	2300 ± 20	100 ± 1	99	90	1.13
E-PCL 4700		0.43 ± 0.01	4700 ± 70	100 ± 1	99	97	1.12
E-PCL 6400		0.32 ± 0.01	6400 ± 40	101 ± 2	100	99	1.16
E-PCL 8700		0.23 ± 0.02	8700 ± 400	100 ± 5	99	98	1.18

[a] Average ± standard deviation. Measurements performed in triplicate.

It should be noted that this synthetic approach was selected due to its high degree of control, robustness and scalability. Indeed, having a well defined network is crucial to draw accurate conclusions. Furthermore, scalability is critical when considering volumetric 3D-printing and commercialization of ready-to-use (bio)ink formulations. The herein reported synthetic approach could be scaled-up to kilogram-scale, while maintaining excellent control over the product. Finally, well-defined systems are preferred when taking regulatory considerations into account. To the best of our knowledge, this is the first time that this approach has been reported as a means to introduce alkenes onto PCL. Compared to the state-of-the-art, functionalization of PCL with cross-linkable groups (i.e., acrylates) is usually performed via diisocyanate linkers such as isophorone diisocyanate (IPDI).[26–29] However, this often results in low degree of control due to the occurrence of repeating units within the central backbone, resulting from the low selectivity towards one of both isocyanates. Another widely described approach for the functionalization of hydroxyl-terminated polymers end-capped with acrylates involves the use of acid chlorides (i.e., acryloyl chloride). While this approach results in highly controlled

acrylate-functionalized PCL, the resulting brittleness of acrylate-cross-linking limits its applicability (*vide infra*).[30–32]

2.2. Design and characterization of thiol-ene photo-crosslinked PCL networks

By means of the synthesized PCL precursors, thiol-ene photo-cross-linked networks with varying M_c could then be obtained. To do so, the synthesized precursors were combined with the tetra-functional thiol (pentaerythritol tetrakis(3-mercaptopropionate)) and ethyl (2,4,6-trimethylbenzoyl) phenyl phosphinate (TPO-L) as photo-initiator. After UVA-irradiation, very elastic, cross-linked networks (i.e., elastomers) were obtained, that swiftly crystallized to form tough and hard materials. Interestingly, although the designed networks are cross-linked, the materials maintain the ability to undergo melting-crystallization cycles, similar to thermoplastic PCL which is a semi-crystalline polymer. This is important to note since the introduction of cross-links generally restrict the mobility of the polymer chains, and as a result, impedes crystallization. Here, the ability to undergo melting-crystallization cycles while being cross-linked is attributed to the telechelic nature of the PCL precursors, the relatively low cross-link density and the homogeneous network topology concomitant with thiol-ene cross-linking (*vide infra*). As a result, the herein reported materials are semi-crystalline cross-linked networks, a class of materials of which only few are reported to date.[33]

Subsequently, thorough characterization of the formed networks was performed. First, gel fraction and swelling experiments were carried out. Gel fractions ranged between 92 and 98%, illustrating excellent network interconnectivity. The swelling degree provides initial insight into the network structure and the effect of the altered cross-link density (i.e., M_c). For hydrogels, this relationship is well-established by means of the so-called equilibrium swelling theory.[34] Here, we found a correlation between M_c and the degree of swelling of the networks. More precisely, from the lowest to highest molar mass, the mean swelling degree increased by 96% (Table 2). Given the fact that the gel fraction is high for all networks, it is evident that these changes in swelling behavior result from the differences in M_c. All swelling degrees differed

significantly ($p < 0.05$) from each other, except for E-PCL 6400 and E-PCL 8700. The observed correlation can be explained by the homogeneous network topology that is associated with thiol-ene cross-linking chemistry. The more homogeneous network topology, as compared to acrylate-cross-linked networks, has been illustrated by other researchers and stems from the polymerization mechanism (i.e., step-growth *versus* chain-growth polymerization).[25] To benchmark the obtained results throughout this work, acrylate cross-linked PCL networks were synthesized with M_n of 2900 (A-PCL 2900) and 8400 g.mol^{-1} (A-PCL 8400) (Figure S4-S5). For the acrylate crosslinked networks, swelling ratios of 3.9 ± 0.2 and 7.0 ± 0.1 were obtained, respectively. These results illustrate that the acrylate crosslinked PCLs swell significantly less compared to the thiol-ene crosslinked PCLs, as could be expected given their inhomogeneous network topology.[23]

Next, the double bond conversion (DBC) during network formation was investigated via differential photo-calorimetry (DPC) and high-resolution magic-angle spinning (HR-MAS) ^{1}H-NMR spectroscopy. These techniques were used, instead of more conventional infrared spectroscopy (FTIR), as the relatively low concentration of cross-linkable groups and the presence of noise stemming from the polymeric backbone render FTIR spectroscopy inappropriate. DPC is a technique via which it is possible to determine the DBC based on the reaction heat that is released during cross-linking. More precisely, through determination of the released reaction heat at a certain point in time, and the total heat that is released upon full conversion, the double bond conversion throughout the cross-linking process can be monitored. Via DPC, final DBCs of 80, 75, 85 and 69% were determined for networks based on M_c of 2300, 4700, 6400 and 8700 g.mol^{-1}, respectively (Figure 2D).

To further verify these results, HR-MAS NMR spectroscopy was performed. Similarly to conventional MAS-NMR spectroscopy, the sample is rotated while being positioned at the magic angle. However, due to the fact that the samples to be analyzed are swollen, the same pulse programs as for conventional liquid state NMR spectroscopy can be used, which reduces

peak broadening in HR-MAS NMR spectroscopy as compared to MAS NMR spectroscopy. As a result, the former is an excellent technique to determine the fraction of un-reacted alkenes in the cross-linked networks. To do so, the spectra were normalized according to the protons that correspond to the central ethylene glycol moiety (n = 2, 4.2 ppm) that was used to initiate the PCL polymerization (Figure S6). Integration of the alkene proton (n = 1, 5.8 ppm) then provides insight in the percentage of alkene functionalities that remained un-reacted (Figure 2E). By doing so, final double bond conversions (DBCs) of 87, 90, 80 and 86% were determined for networks based on M_c of 2300, 4700, 6400 and 8700 g.mol^{-1}, respectively.

Interestingly, DBCs determined via HR-MAS NMR spectroscopy were found to be higher than those determined via DPC. These differences can be explained in different ways. First, in DPC, a correction must be applied to account for the heat that corresponds to the irradiation source (Figure S7). Because of this correction, a fraction of the initial reaction heat is lost. Secondly, in DPC, the calculated DBC is based on a model reaction. Indeed, the fact that the model system is not identical to the actual polymeric system is also expected to contribute to the observed differences. As model reaction, the reaction between diallyl phthalate and PETA-4SH was selected, based on which a reaction enthalpy of 71 kJ.mol^{-1} (i.e., 19.7 kcal.mol^{-1}) was calculated (Figure S8). This reaction enthalpy corresponds well with values reported in literature for small-molecule thiol-ene systems and is slightly smaller compared to acrylates' reaction enthalpy (77.6 kJ.mol^{-1}).[35] In addition to the aforementioned aspects, also some additional points regarding the DBC have to be noted. First, due to the large molar mass difference between the PCL precursor and the thiol cross-linker, in addition to the higher functionality of the latter (n = 4), only small amounts of PETA-4SH are needed to create stoichiometric networks (i.e., thiol to ene ratio of 1). Secondly, said stoichiometric thiol-ene ratio was based on the assumption that disulfide bonds were absent. Thus, any presence of disulfide bonds would reduce the final DBC. Lastly, as the conversion increases, limited chain and small molecule mobility can be expected to contribute to the observed incomplete conversion of the double bonds. However,

taking these considerations into account, final DBCs were found to be high and were generally ranging between 80-90%. These results illustrate that orthogonal thiol-ene chemistry is an excellent strategy to cross-link PCL oligomers, in a rapid fashion while reaching high DBC. Indeed, when these results are compared to the state-of-the-art, the herein reported DBCs are in line with those reported for thiol-ene reactions based on small molecules.[36–39]

Subsequently, the evolution of the shear moduli (i.e., G' and G'') during network formation was investigated via photo-rheology. It should be noted that photo-rheology is performed above the melting temperature of the materials (*vide infra*). As a result, the materials considered here are completely amorphous. Based on photo-rheology, no clear effect of M_c on the gelation point (i.e., cross-over between G' and G'') could be identified (Figure 2C). However, a slight increase of the gelation point can be observed for E-PCL 8700, possibly indicating that higher molar masses would slightly delay gelation (Table 2). Furthermore, as the cross-link density was reduced, the post-polymerization storage modulus (G') decreased (Figure 2A). Indeed, this could be expected as the cross-link density and shear modulus (G') are directly related according to the rubber elasticity theory for ideal networks.[40] Ideal networks are networks that are composed of narrowly dispersed strands and equally branched cross-links.[40] Interestingly, if one assumes full conversion and the absence of network defects, the thiol-ene networks reported herein can be considered ideal networks and the rubber elasticity theory would apply (Figure 2B). This is due to the homogeneous network topology stemming from the step-growth polymerization mechanism (i.e., thiol-ene cross-linking). Given that the degree of substitution (> 99%) and double-bond conversions (> 80%) were shown to be high and that chain-end defects can be accounted for by introduction of a factor γ, these assumptions seem reasonable. The relationship between G' and M_c, according to the rubber elasticity theory, is given by:

$$G' = \frac{\rho RT}{M_c}\left(1 - \frac{2}{f}\right)(1 - \gamma) \qquad (1)$$

In this equation, ρ refers to the network density, R is the universal gas constant, T is the absolute temperature, f is the cross-linker functionality, γ is a universal structural parameter to account for chain-end defects and M_c is the molar mass between cross-links (Figure S9).[40] If we then apply said relationship to the cross-linked PCL networks, we obtain a near-perfect match between theoretical and experimental shear moduli, while maintaining the universal structural parameter equal to zero (Table 2). These results indicate that near-ideal PCL based networks, that behave according to the rubber elasticity theory are obtained. Finally, M_c can also be calculated theoretically, starting from the experimentally determined shear modulus (G'). If we do so, we see that M_n (determined via ^{1}H-NMR spectroscopy) matches the theoretically determined M_c (based on G'). It should be noted that, in addition to the near ideal network topology resulting from the thiol-ene cross-linking chemistry, these results illustrate the importance of exploiting a synthetic approach for the precursors that is well-controlled.

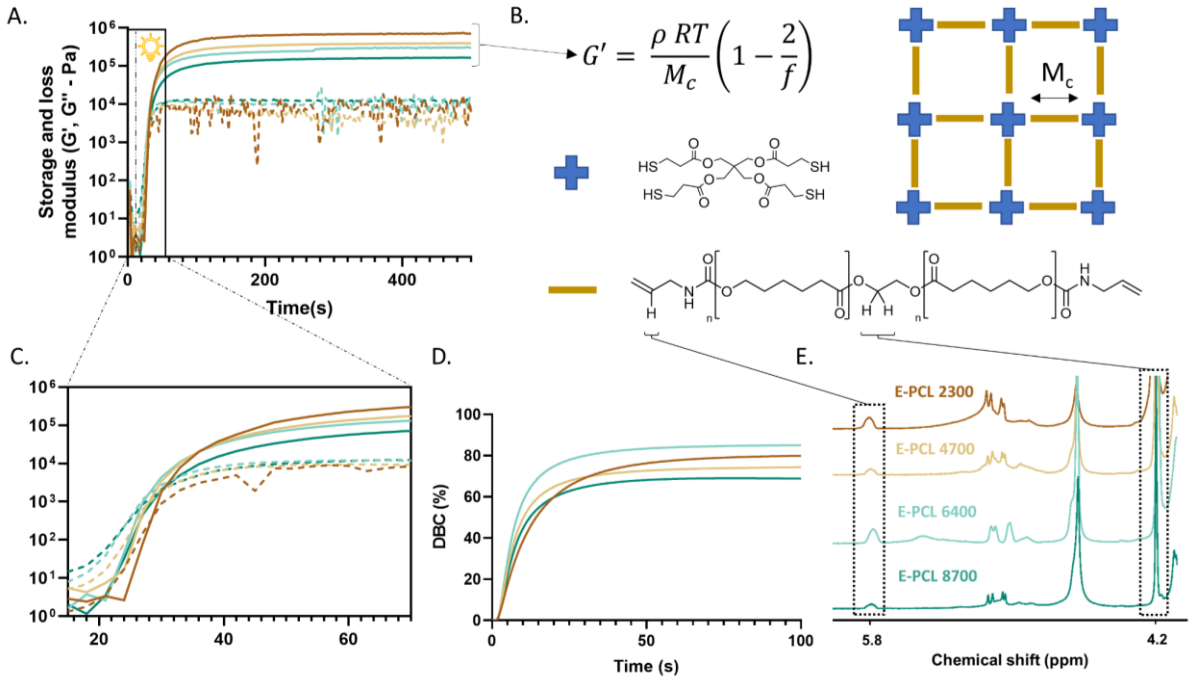

Figure 2. A. Photo-rheology of the PCL networks; B. Schematic description of the obtained near ideal PCL networks and relationship between the shear modulus (G') and the network architecture as provided by the rubber elasticity theory; C. Zoom of the gelation points obtained by photo-rheology of the different networks; D. Double bond conversions (DBC) as determined

by differential photo-calorimetry (DPC); E. HR-MAS ^{1}H-NMR spectra used to determine DBC. As illustrated, the spectra were normalized according to the initiator's methylene moiety (4.2 ppm) and the DBC was determined based on the signal intensity corresponding to the residual unreacted alkene moieties (5.8 ppm).

Table 2. Gel fraction, swelling ratio, gelation point, theoretical and experimental storage moduli (G') and M_c of the various thiol-ene photo-cross-linked PCL networks.

#	Gel fraction (%) [b]	Swelling ratio [b]	Gelation Point (s) [b]	Exp. Storage Modulus (G' – MPa) [b]	Theor. Storage Modulus (G' – MPa)	M_c (g.mol^{-1}) [b]
E-PCL 2300	97.7 ± 2	7.4 ± 0.1 [a]	13.3 ± 0.3	0.77 ± 0.11	0.70	2100 ± 300
E-PCL 4700	95.2 ± 2	9.3 ± 0.4 [a]	12.3 ± 0.2	0.47 ± 0.12	0.34	3600 ± 1100
E-PCL 6400	92.3 ± 2	13.4 ± 0.4	13.5 ± 0.6	0.26 ± 0.04	0.25	6200 ± 1000
E-PCL 8700	95.8 ± 1	14.5 ± 0.6	14.8 ± 0.3	0.17 ± 0.01	0.18	9500 ± 200

[a] significantly different ($p < 0.05$, E-PCL 2300, 4700 and 6400).[b] Average ± standard deviation.

2.3. Thermal properties and influence of M_c

Thermal properties of the cross-linked network such as the crystallinity and degradation temperature are important physical characteristics. This is because they influence, among others, the mechanical properties and provide insight into the materials' behavior at body temperature. To assess the influence of the various network architectures on the thermal properties of the materials, thermogravimetric analysis (TGA) and differential scanning calorimetry (DSC) were performed.

TGA showed that negligible degradation occurred below 240 °C, illustrating excellent thermal stability of the reported materials (Table 3).

Furthermore, via DSC, a clear correlation between M_c and the crystallization/melting behavior of the materials was observed (Table 3). More precisely, as M_n increased from 2300 to 8700 g.mol^{-1}, the melting temperature and enthalpy increased from 30 to 51°C and 46 to 63 J.g^{-1}, respectively (Figure 3A). The observed behavior can be explained by the fact that the cross-

links reside in the amorphous regions situated in-between the PCL lamellae. As M_c increases, longer uninterrupted PCL chains are present, that can form longer uninterrupted crystalline segments, thereby increasing the melting temperature and enthalpy.[41]

When these results are compared to those of thermoplastic PCL (i.e., PCL 80 000 $g.mol^{-1}$), it can be seen that PCL precursors with M_c above 2300 $g.mol^{-1}$ lead to networks with comparable melting temperatures and enthalpies (Table 3).[15] Interestingly, the majority of the melting temperature increase occurs when M_c is increased from 2300 to 4700 $g.mol^{-1}$. This finding has important implications in a biomedical context, given that body temperature is 37 °C. As a result, a network based on E-PCL 2300 would not remain crystalline upon implantation in the body, which is expected to affect its mechanical performance. However, PCL networks based on higher M_c would remain crystalline upon implantation. Therefore, said precursors would be preferred if mechanical stability is paramount. Nevertheless, E-PCL 2300 might be an interesting candidate for applications where shape-memory behavior, driven by the crystalline to amorphous transition, is desirable. However, more research is needed to verify said behavior, which is beyond the scope of this work.

Table 3. Degradation temperature, crystallization temperature and enthalpy, melting temperature and enthalpy as well as crystallinity (χ) of the various PCL networks determined via TGA and DSC.

#	$T_{d,98\%}$ (°C)	T_c (°C) [a]	ΔH_c (J/g) [a]	T_m (°C) [b]	ΔH_m (J/g) [b]	χ (%) [b]
E-PCL 2300	240	-12	47	30	46	34
E-PCL 4700	248	13	57	48	59	43
E-PCL 6400	244	17	60	51	62	45
E-PCL 8700	251	20	60	52	63	46
A-PCL 2900	285	-31	21	22	25	18
A-PCL 8400	285	16	55	49	54	40

PCL 80 000	340	21	57	55	52	38

[a] First cooling run. [b] Second heating run.

2.4 Degradation rate and influence of M_c

In a biomedical context, to be able to control or select a certain biodegradation rate is of great interest. In targeted drug delivery, the rate of release of active pharmaceutical ingredients can be controlled by tuning the degradation rate of the polymeric drug delivery vehicle.[42] In regenerative medicine, it is often the goal to replace a degrading scaffold by regenerated tissue.[43]

In this context, the materials' degradation rates were investigated, and more specifically, the influence of M_c on those degradation rates. To do so, an accelerated degradation assay (i.e., upon exposure to 5 M NaOH) was performed (Figure 3B). Interestingly, these results illustrate a strong dependence of the degradation rate on M_c. More precisely, a higher cross-link density (i.e., reduced M_c) was found to accelerate degradation. After 4 days, E-PCL 2300 was found to be fully degraded. While for E-PCL 4700, 6400 and 8700, the residual mass (after 10 days) accounted to 27, 47 and 73%, respectively. Moreover, the degradation rates in accelerated conditions, were significantly higher compared to those of thermoplastic PCL (i.e., PCL 80 000), which showed limited degradation after 10 days (89 % remaining mass).

When looking at the chemical structure of the cross-linked networks, different chemical functionalities can be observed that are susceptible to hydrolysis. Namely, the urethane functionalities generated during the PPM, the ester bonds present in the PCL backbone and the ester bonds present in the cross-linker. However, as the rate of hydrolysis for urethanes is significantly slower compared to esters, urethane degradation is expected to be negligible.[44] Moreover, given the clear correlation between the degradation rate and the cross-link density, it is reasonable to assume that the cross-links are involved in the observed degradation. Interestingly, previous research has shown that ester functionalities with a neighboring thio-ether linkage are more susceptible to hydrolysis, with the effect being more pronounced when

the spacing between both groups is reduced.[45] Since only two carbon atoms are present between the thioether and ester group in case of the cross-linker, the close proximity of the thioether to the ester is expected to increase its susceptibility to hydrolysis, as compared to the ester-functionalities present in the PCL backbone. In addition, the crystallinity of the materials can further explain the observed trend. Indeed, due to the close packing of the lamellae, crystalline regions degrade more slowly as compared to amorphous regions. Therefore, as the crystallinity of the PCL networks increases, upon increasing M_c (*vide supra*), the degradation can be expected to delay.

Given the observed differences of the degradation rate under accelerated conditions, insight into the degradation rate under physiological conditions is important to delineate possible applications of the herein reported materials more clearly. Therefore, to simulate physiological conditions, the materials were degraded for a duration of one month, in phosphate buffered saline (PBS) at 37°C (Figure 3C). In general, after a period of one month, close to no degradation (i.e., weight loss) was observed for any of the networks. These results illustrate that, while the degradation was considerably faster under accelerated conditions, the degradation in physiological media is much more similar to thermoplastic PCL. As a consequence, the herein reported materials would be suitable for similar applications as compared to conventional thermoplastic PCL, including long-term implantable devices. Interestingly, while a one month degradation resulted in a weight loss of 1.1 ± 0.5 % in case of the thermoplastic PCL, a slight weight gain (1-2%) was observed for the cross-linked networks (Figure S10). The observed weight increase is attributed to minimal water uptake of the networks. This is attributed to the increased hydrophilicity of the networks as compared to thermoplastic PCL, due to the incorporation of the cross-linker. Indeed, albeit non-significant, an increase of the hydrophilicity was seen for the most densely cross-linked network via static contact angle measurements, tested prior to degradation (Figure S11). While caution should be advised, these results indicate that bulk degradation could take place to some extent in the cross-

linked networks, which could further explain the observed differences seen under accelerated conditions.

In conclusion, the degradation rate of the herein reported materials can be tuned, by means of M_c. Yet, the degradation in physiological conditions is still relatively slow and it is reasonable to assume that complete degradation in physiological conditions would take considerably longer than rapidly degrading polyesters such as poly(lactic acid).[9] As a result, the herein reported materials would be suitable for the development of long-term biodegradable implants, similarly to thermoplastic PCL.

2.5. Mechanical properties and influence of M_c

In addition to their degradability, their superior mechanical properties are one of the main advantages that synthetic polyesters have over natural polymers. Indeed, mechanical performance is crucial in the context of biomedical applications as scaffolds should be able to withstand the respective mechanical load at the defect site, and it is in this context that acrylate-cross-linked materials generally perform suboptimal. Moreover, it is reasonable to assume that said suboptimal performance of acrylate cross-linked polymers contributes to the fact that light-based 3D-printing is still applied relatively infrequently for the reconstruction of (load-bearing) hard tissues compared to extrusion-based 3D-printing (where thermoplastic PCL can be used). Here, we evaluated the mechanical performance, and influence of M_c on said performance, via tensile testing. Furthermore, we benchmark the obtained results to thermoplastic PCL (PCL 80 000), the gold standard in extrusion 3D-printing of PCL. Additionally, the herein reported materials are compared to acrylate cross-linked PCL (A-PCL), the gold standard for light/projection-based 3D-printing of PCL.

When evaluating the influence of M_c on the mechanical properties, several interesting trends can be observed (Figure 3D). As the cross-link density is reduced (i.e., increasing M_c), the Young's modulus, yield strength, elongation at break and ultimate strength increase (Table 4). The inverse relationship between the Young's modulus and the cross-link density may seem

counterintuitive, as more densely cross-linked networks are generally associated with an increase in modulus. Indeed, this statement holds for elastomers (i.e., amorphous networks). However, as introduced before, the herein reported materials are still able to undergo melting-crystallization cycles after cross-linking, and thus, are semi-crystalline during tensile testing (similarly to PCL 80 000). Therefore, while it was shown by photo-rheology that reducing M_c led to an increase of G' for the non-crystallized materials (*vide supra*), the observed Young's modulus during tensile testing is rather governed by the crystallinity of the materials. This is illustrated by the clear correlation between the cross-link density and the material's crystallinity, which is further confirmed when considering the acrylate cross-linked PCLs and PCL 80 000 (Table 4).

When looking at the stress-strain curves, significant plastic deformation can be observed, which becomes more pronounced as M_c increases. Interestingly, similar behavior is observed for PCL 80 000, illustrating that the behavior of the cross-linked networks is comparable to that of a tough plastic (i.e., thermoplastic with significant chain entanglements) (Figure 3D). However, in case of PCL 80 000, the high elongation at break and toughness result from long entangled polymer chains that connect several lamellae together by traversing the amorphous regions in between the spherulites.[41,46] In case of the cross-linked networks, M_n (or M_c) is too low for significant chain entanglements to be present. Here, it is assumed that the individual lamellae are connected together by cross-links that reside in the amorphous regions. As the polymer is deformed, extensive reorganization of the spherulites and network takes place, during which the polymer segments that connect the cross-links are extended and oriented in the direction of stretch. It should be noted that the extension and orientation in the direction of stretch is typical for rubbers (i.e., cross-linked amorphous materials).[47]

When the observed behavior is compared to acrylate-cross-linked PCL, important differences can be noted (Figure 3E, 3F). Most importantly, when comparing networks based on precursors with similar M_n, the elongation at break is significantly lower for the acrylate cross-linked

networks. Indeed, in case of A-PCL 2900, brittle behavior was observed characterized by an elongation at break and ultimate strength of only 20 ± 10 % and 1.4 ± 0.5 MPa, respectively (Table 4). This 18- and 10-fold difference, respectively, can be explained by the network topology that is concomitant with acrylate cross-linking. Acrylate cross-linked networks have inhomogeneous spatial distribution of cross-links throughout the network (i.e., high and low cross-link density regions are formed).[25,36] This inhomogeneous distribution of cross-links is hypothesized to limit the ability of the polymer chains in between the cross-links to reorient in the direction of stretch. When the molar mass is increased to 8400 $g.mol^{-1}$, the same effect can be seen, albeit less pronounced. Moreover, said limited mobility is hypothesized to prevent crystallization in case of A-PCL 2900, which in turn explains the lower yield strength and Young's modulus that were observed. However, it should be noted that A-PCL 8400 also crystallized, resulting in a similar yield strength and Young's modulus. These results illustrate that, when the yield strength is considered, the thiol-ene networks based on the lowest M_c illustrate the largest improvements over the acrylate cross-linked networks. Finally, it can be hypothesized that elastic materials (i.e., elastomers) could be obtained if the crystallization of the thiol-ene cross-linked materials could be suppressed which can be considered interesting future work.

To summarize, M_c is illustrated to be an excellent tool to control the mechanical behavior of cross-linked networks, which is especially relevant for homogeneous networks (i.e., thiol-ene cross-linking) as they can overcome the brittleness concomitant with acrylate cross-linking. Finally, when considering suitable applications for the herein reported materials, reconstruction of moderate to stiff tissues (i.e., cartilage and bone tissue) should be considered. In this context, the importance of the yield strength should be noted. Indeed, beyond the yield point, permanent deformation takes place, impacting the shape fidelity of the implant. Therefore, when the yield strength is considered, it can be concluded that the performance of the thiol-ene cross-linked networks is similar to PCL 80 000, which is currently used in several tissue engineering

treatments that are available on the market, yet cannot be processed via light-mediated 3D-printing techniques.[15]

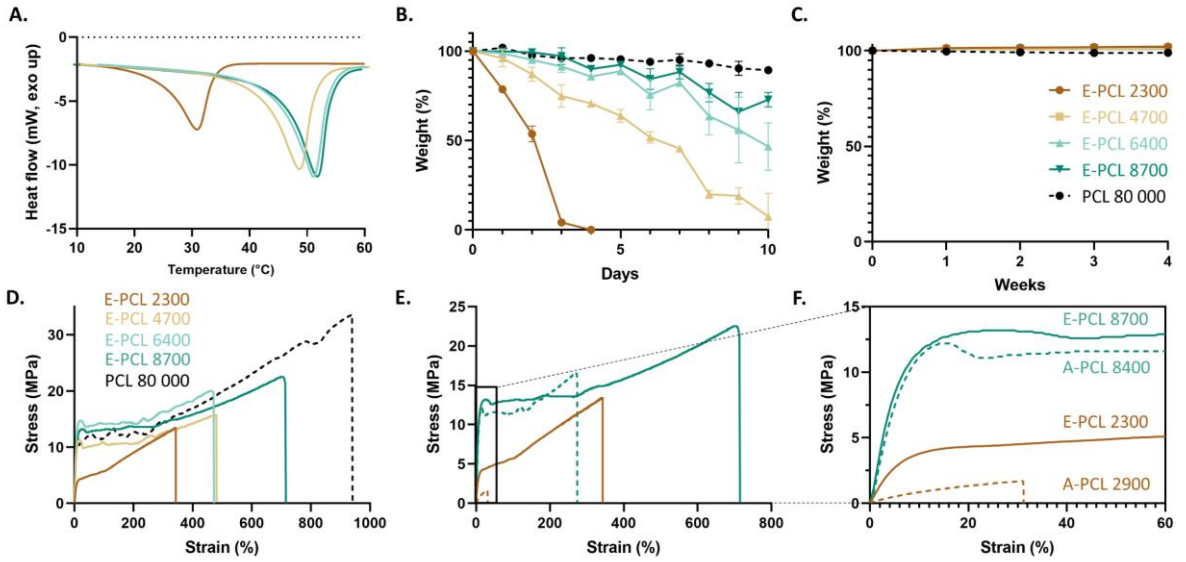

Figure 3. A. DSC Thermograms, based on the second heating run, of the PCL networks; B. Accelerated degradation assays of the PCL networks in 5 M NaOH; C. Degradation of the PCL networks in physiological conditions (PBS, 37°C); D. Stress-strain curves obtained via tensile testing of the PCL networks with thermoplastic PCL (PCL 80 000 - dotted line) as benchmark; E. Stress-strain curves obtained via tensile testing of thiol-ene (solid lines) and acrylate cross-linked PCL (dotted lines); F. Inlet of Figure 3E to highlight the yield points of the acrylate and thiol-ene cross-linked networks.

Table 4. Young's modulus, yield strength, elongation at break, ultimate strength and crystallinity (**χ**) for the different thiol-ene cross-linked PCLs, thermoplastic PCL (PCL 80 000) and acrylate cross-linked PCL (A-PCL 2900, A-PCL 8400).

#	Young's modulus (MPa)[b]	Yield strength (MPa)[b]	Elongation at break (%)[b]	Ultimate strength (MPa)[b]	χ (%)[c]
E-PCL 2300	66 ± 10	4.4 ± 0.5	350 ± 40	14 ± 1	23
E-PCL 4700	177 ± 10	11.0 ± 0.4	470 ± 50	16 ± 1.0	40
E-PCL 6400	252 ± 10	13.8 ± 0.7	410 ± 60	21 ± 3	53

E-PCL 8700	215 ± 20	13.4 ± 0.5	630 ± 100	23 ± 3	52
A-PCL 2900	10 ± 1	N.A. [a]	20 ± 10	1.4 ± 0.5	3
A-PCL 8400	196 ± 20	12.2 ± 0.1	280 ± 30	17 ± 2	35
PCL 80 000	233 ± 10	13.2 ± 0.7	950 ± 140	34 ± 4	42

[a] N.A. = not applicable. [b] Average ± standard deviation. [c] First heating run.

2.6 Volumetric 3D-printing (VP)

Interconnected porous scaffolds are crucial to enable tissue ingrowth and patient-specific implants (PSIs) have been shown to reduce operation times, reduce tissue damage during implantation and reduce post-operational infections as a result of the excellent fit with the anatomical structure.[2,3,48] Yet, a method by which a PSI can be manufactured rapidly, accurately, and on-site in a sterile environment has remained elusive. In this context, volumetric 3D-printing (VP) has recently been introduced as the first truly volumetric 3D-printing technique (i.e., volume-at-once) and can be considered the ideal manufacturing technique (Figure 4A).[4] Interestingly, for a given resin container and projection system, the manufacturing time is independent of the size or geometry of the object to be printed, rendering it significantly faster as compared to other (light-based) 3D-printing techniques, while maintaining µ-scale resolution.

In order for the resin to be printable, it should be transparent at the illumination wavelength. Given the significant scattering of the crystalline domains of PCL, the materials can only be printed while being amorphous or dissolved. As a result, the developed materials could either be 3D-printed while heated (i.e., molten) or by means of an organic solvent to dissolve the PCL precursors. Here, we opted for the use of organic solvents given the operational difficulties associated with 3D-printing in a heated (refractive index matching) bath (Figure S12). However, VP in thermal mode would be an interesting direction for future research as it would exclude the need for solvents and would be preferable from regulatory and environmental perspectives.

As suitable organic solvent, chloroform, toluene and dimethyl formamide (DMF) were investigated, given their PCL solubilization capacity. It should be noted that it is important to minimize the amount of solvent that is introduced, as the introduction of solvent lowers the viscosity of the resin. When the viscosity of the resin is lowered too much, sinking of the object during 3D-printing can occur. This is due to the fact that the polymerization leads to a locally increased density. Therefore, to select the most suitable solvent, the resulting viscosity and influence on the DBC were taken into account. As toluene and DMF resulted in too low viscosities or introduced cross-linking artefacts, chloroform was selected (Figure S13). Additionally, as VP can be performed within a closed system (i.e., a vial with a cap), volatile solvents can be considered beneficial because they can be readily removed post-printing. In this regard, it should be noted that the use of organic solvents during development of an implant does not restrict its application in biomedical engineering as long as the organic solvent can be effectively removed from the 3D-printed construct. For chloroform in particular, a class two solvent, the guidelines according to the International Council for Harmonisation (ICH) are that the concentration of residual chloroform should be below 60 ppm. In this context, complete removal of the solvent from the 3D-printed constructs was illustrated via TGA (Figure S14). Finally, it should be noted that by the introduction of organic solvents, the tissue engineering approach is restricted to a top-down approach, where cells can only be combined with the scaffold, post-printing.

Next, in order to identify suitable photo-initiator and photo-inhibitor concentrations, an exploratory printability screening of a tubular construct was performed using E-PCL 4700. More precisely, resin formulations consisting of various combinations of TPO-L and (2,2,6,6-tetramethylpiperidin-1-yl)oxidanyl (TEMPO) loadings were evaluated (Figure 4B, Figure S15).[49] These results indicate a clear relationship between the TPO-L *versus* TEMPO loading and the required projection time. As expected, increasing the TPO-L concentration led to a reduction of the required projection time, while increasing the TEMPO concentration led to an

increase of the required projection time. Based on the outcome of the tubular constructs, three regimes could generally be distinguished (Figure 4C). Too short projection times resulted in an under-cured blob of very sticky and elastic material having a collapsed central channel. Too long projection times resulted in a solidified central channel. Suitable projection time windows resulted in a tubular construct with sufficient mechanical integrity (illustrated in green). Interestingly, these results show that it is impossible to print the thiol-ene cross-linkable PCL in the absence of TEMPO. Indeed, in the absence of TEMPO, the tubular constructs were either under-cured, resulting in a blob, or over-cured within the central channel prior to sufficient formation of the tubular walls (illustrated in red). Additionally, in the absence of TEMPO, the surrounding resin became very viscous, indicating un-desired curing of out-of-part voxels. Increasing the TEMPO concentration to 0.005 wt.% improved the printability, as the surrounding resin was observed to become less viscous. However, proper development of the central channel only became possible in the presence of 0.01 wt.% TEMPO or more. These results are in line with previous research, in which it has been stated that an inhibition period is crucial to allow for out-of-part voxels to receive a certain light-dose without noticeable curing.[4] In order to introduce this inhibition period into thiol-ene based resins, TEMPO was proposed by Shusteff and co-workers, given that it is a radical scavenger and potent inhibitor of radical-mediated reactions.[50] It should be noted that the addition of TEMPO is not necessarily essential in acrylate-based resins, due to the inherent oxygen inhibition of acrylates (Figure S16). However, since oxygen is generally present within the resin as dissolved gas and its concentration is therefore hard to control, it might be favorable to control the inhibition period by a dissolved radical scavenger such as TEMPO. Finally, excellent agreement was illustrated between the theoretical and experimental length of the tubular constructs, illustrating that limited (solvent-attributed) shrinkage occurred (Table S3).

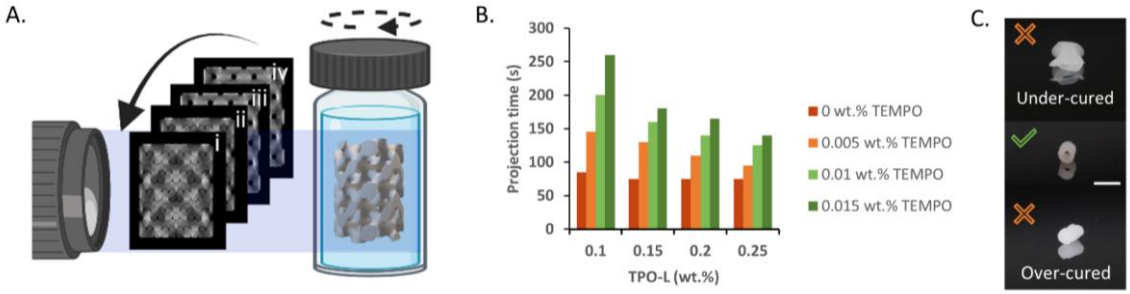

Figure 4. A. Schematic depiction of volumetric 3D-printing (also referred to as computed axial lithography); B. Exploratory printability screening of a tubular construct with various TPO-L and TEMPO loadings; C. Pictures illustrating the three regimes that could be distinguished during the exploratory printability screening being: under-cured (i.e., collapsed central channel), over-cured (i.e., central channel is also cross-linked) and suitable (i.e. mechanically intact and central channel present). Scale bar is 5 mm.

Of further interest was the influence of the cross-link density (and M_c) on the printability of the materials via VP. In order to investigate this, a diamond lattice structure (having a porosity of 70%) was printed with resins based on the different PCL precursors. It was hypothesized that the scaffolds' porosity would require a certain cross-link density (or M_c) to prevent collapse. Indeed, a very pronounced influence of M_c on the scaffolds' mechanical integrity, and therefore, printability, was observed. More precisely, E-PCL 2300 could be readily printed without collapsing, using conventional post-processing procedures (i.e., washing and post-curing) (Figure S17). To develop porous constructs based on E-PCL 4700, 10 µL of additional TPO-L (3.5 mM) was added during the post-curing to ensure sufficient conversion of the double bonds (Figure S18). Scaffolds based on M_n exceeding 4700 g.mol^{-1}, on the other hand, collapsed as soon as the solvent evaporated (Figure 5A). These results clearly illustrate that a certain critical M_c is required in order to withstand gravitational and surface-tension driven collapse. For the reported materials, said critical M_c is situated between 4700 and 6400 g.mol^{-1}. Moreover, based on the photo-rheology measurements (*vide supra*), said range can be translated into a shear-

modulus (upon full conversion) that is situated between 415 and 222 kPa. These results highlight a fundamental problem when complex (porous) structures are to be printed using low-modulus materials (which is often the case for hydrogels for example). Interestingly, we have elaborated a strategy by which this fundamental problem can be overcome and the low-modulus PCL precursors could be printed as well, without collapsing. More precisely, by gradually replacing the washing solvent with a very incompatible solvent (with respect to the PCL precursors), we induced crystallization while the structure was still immersed in solution (Figure 5A, S19). As a result of the formation of crystalline domains and the corresponding increase in Young's modulus, the scaffold is able to resist gravitational and surface tension-driven collapse upon removal of the solvent. As a result, the proposed strategy enables complex (highly porous) objects to be volumetrically printed using low-stiffness precursors (Figure 5B). It can be considered interesting future work, to expand this concept towards other semi-crystalline polymers.

Next, we considered the materials' volumetric printability for highly complex objects using E-PCL 2300. To illustrate the excellent volumetric printability, several complex geometries were 3D-printed, including a perfusable vasculature with a central channel of 900 µm and a wall thickness of 400 µm (Figure 5C). Additionally, highly porous strut-like cubic and octahedron lattices with strut diameters of 100 µm were volumetrically printed (Figure 5D). Notably, these feature sizes can be considered the smallest features printed to date via CAL, with non-acrylate based-resins.

As was discussed, to print the developed materials via VP, introduction of a small amount of chloroform (10-20 v%) and TEMPO (0.1 mg/mL) are crucial. In addition, the TPO-L concentration (0.12 wt.% instead of 0.25 wt.%), delivery of the light dose (i.e., small dose during VP, followed by post-curing) and light intensity (8 mW/cm² instead of 5 mW/cm²) are different when compared to the melt-casted materials that were characterized in-depth (*vide supra*). Therefore, it was illustrated that the volumetrically printed materials have similar

properties to the melt-casted materials, as evidenced through tensile testing, DSC and TGA analysis, performed on 3D-printed constructs based on E-PCL 6400 (Figure S20).

Finally, to provide insight into the evolution of the mechanical properties during degradation of volumetrically printed constructs, dog bones were film-casted starting from resin compositions used during VP. After degradation in physiological environment (PBS, 37°C) for a duration of one month, the dog bones were analyzed via tensile testing (Figure S21). Interestingly, after degradation, it was seen that the yield strength and Young's modulus of the PCL networks increased, while the elongation at break was found to be lowered. The increased yield strength and Young's modulus can be attributed to secondary crystallization that has taken place during the time that the 3D-printed object was implanted. Secondary crystallization is a known phenomenon for PCL, and, as the yield strain remained unchanged, these results illustrate that the mechanical performance of the degraded materials remain excellent in view of their use as long-term implants for the reconstruction of moderate to stiff tissues.[51,52] However, thorough investigation of the degradation and the concomitant evolution of the mechanical properties was considered beyond the scope of the current work.

To conclude, in this work, VP of synthetic biodegradable polymers is illustrated for the first time and the smallest feature sizes to date are reported, for non-acrylate based materials. Furthermore, while the resolution of VP is similar to digital light processing (DLP) and stereolithography (SLA), VP is considerably faster. This is illustrated by the printing times that were below 190 s for all resin compositions and geometries. As a result, VP can be considered ideal as a benchtop technique within a hospital, by which PSI could be obtained within a timeframe acceptable to proceed during surgery. Finally, building on the results of this study, the combination of the reported poly(esters) with aqueous resins to create hybrid materials would be an interesting direction for future research. If combined with, for example cross-linkable gelatin, cell-interactive and mechanically stable constructs could be obtained. In this regard, the possibility to overprint existing structures is a crucial advantage of VP.

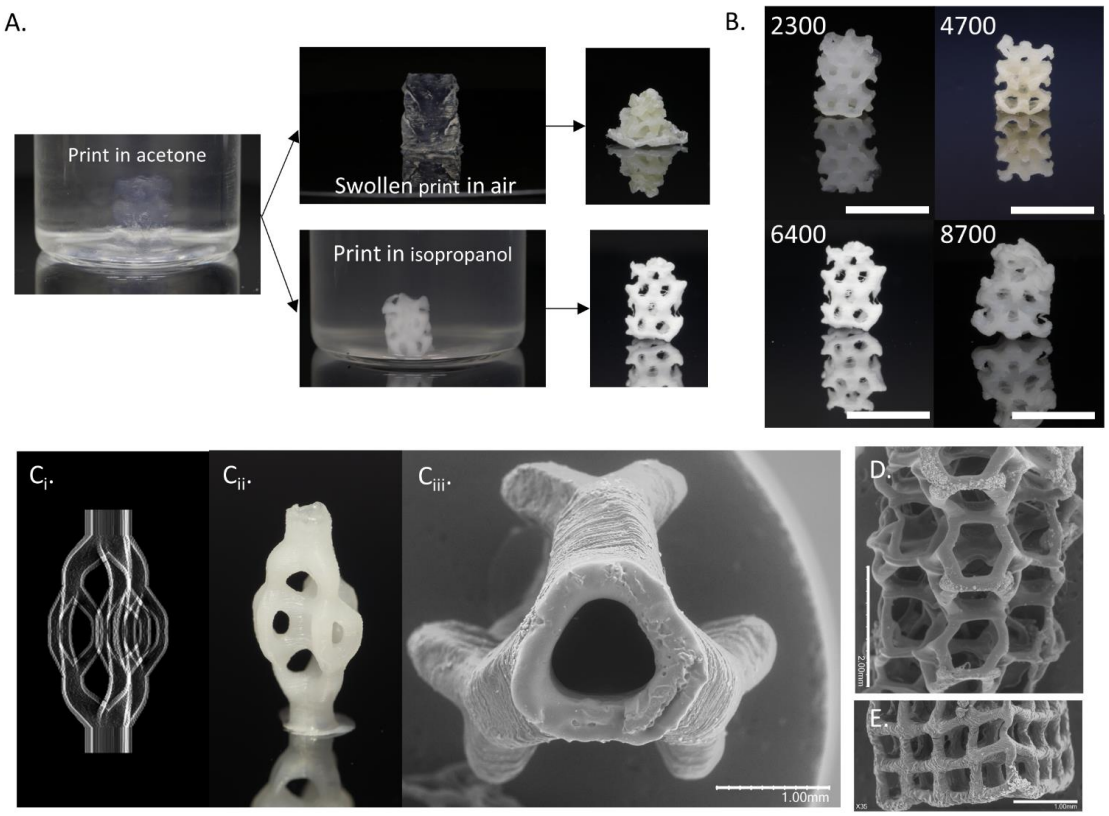

Figure 5. A. Illustration of the strategy that was introduced to volumetrically print loosely cross-linked networks, by means of inducing crystallization to the green part; B. Diamond lattice scaffolds with a porosity of 70% that were volumetrically printed with PCL precursors of varying M_c. Scale bar 5 mm; C. Projection ($_i$), photo ($_{ii}$) and SEM-image ($_{iii}$) of triple vasculature structure that was printed volumetrically with E-PCL 2300. The vasculature has a central channel of 900 µm and a wall thickness of 400 µm. Scale bar 1 mm (Figure S36); D. Strut-like octahedron lattice volumetrically printed with E-PCL 2300. Strut size is 100 µm and scale bar 2 mm; E. Strut-like cubic lattice volumetrically printed with E-PCL 2300. Strut size is 100 µm and scale bar 1 mm.

2.7 Evaluation of the biocompatibility and cytotoxicity of volumetrically 3D-printed constructs

During preclinical evaluation of biomedical implants, illustration of the biocompatibility of the implant is of paramount importance. In this context, *in-vitro* and *in-vivo* evaluation of the biocompatibility of volumetrically 3D-printed constructs, based on the various PCL precursors,

were carried out. To do so, rectangular bars (15 x 3 x 2 mm) were 3D-printed volumetrically, starting from the different PCL precursors (Figure S22). As benchmark, thermoplastic PCL (PCL 80 000), was melt-casted into comparably sized constructs. It should be noted that the use of PCL for several medical applications is approved by the Food and Drug Administration (FDA), while PCL is declared non-toxic and biocompatible according to ISO-10993.[15]

Firstly, the constructs were evaluated in direct contact with adipose tissue-derived stem cells (ASCs). The viability of the cells was assessed via live/dead assays and their metabolic activity via MTS assays, both performed after 1, 3 and 7 days of direct contact with the 3D-printed constructs. These results illustrated excellent biocompatibility of the 3D-printed constructs with viabilities exceeding 99% at all timepoints (Figure 6A). No significant differences were observed between the thiol-ene cross-linked PCLs, the thermoplastic PCL benchmark (i.e., PCL 80 000 $g.mol^{-1}$) and tissue culture plastic (TCP). Moreover, after 7 days of direct contact, the healthy and metabolically active ASCs, as illustrated by the MTS assay (Figure 6B), formed confluent monolayers of cells (Figure S23). While the live/dead and MTS assays clearly illustrated healthy and metabolically active ASCs, the varying MTS response should be noted. Said variation can be attributed to the experimental set-up of the experiment. As the 3D-printed constructs were placed on top of the ASCs, it can be expected that slightly varying gravitational loadings were exerted onto the ASCs.

Moreover, the biocompatibility of the 3D-printed constructs was evaluated in vivo. To do so, the 3D-printed implants were subcutaneously implanted in immune competent BALB/c mice for a duration of one month (Figure 6C). Throughout the duration of the experiment, all mice remained active, grooming and no signs of distress were observed, in any of the groups. Furthermore, the weight of the mice, a general health marker, was evaluated 14 and 30 days after implantation, and no differences were observed between any of the groups (Figure S24).[53] Finally, after implant extraction, necropsy and histopathological evaluation of the mice's organs (kidney, liver and spleen) was performed, illustrating that no systemic reaction was

evoked by the 3D-printed implants (Figure S25). Moreover, when considering the mass and size of the spleen, no increase was observed in any of the groups, which would have been an indication for immune activation (Figure S26-27).[54] Histopathological evaluation of the implants was then performed, which illustrated that the 3D-printed constructs were lined by a thin layer of fibroblasts, having a thickness of approximately 10-30 µm, in which only limited immune cell infiltration was observed (Figure 6E). In this regard, it should be noted that a minimal foreign body reaction (FBR) is considered beneficial as it leads to the production of growth factors (i.e., VEGF) that are critical in the context of vascularization.[55] In terms of FBR, no differences were observed between the 3D-printed constructs and the benchmark (PCL 80 000 $g.mol^{-1}$) as the thickness of the cell layer lining the implants were comparable (10-30 µm) (Figure S28). Neighbouring this thin layer, healthy subcutaneous fat tissue was observed. Interestingly, a significantly enhanced FBR was observed to the polyglactin suture (copolymer of poly(glycolic acid) and poly(lactic acid)) that was used to close the wound which was made during implantation of the 3D-printed constructs. This enhanced FBR was very evident by the increased immune cell infiltration as well as by the increased thickness of the lining cell layer (> 157 µm) as compared to the 3D-printed constructs and thermoplastic PCL (Figure S29). Finally, when considering the in-vivo degradation of the 3D-printed constructs, very limited degradation was observed after being implanted for one month (Figure 6D). The 3D-printed constructs and PCL benchmark did not show any visual signs of degradation and the remaining weight varied between 99-100%. These results correspond well with the degradation rate of thermoplastic PCL reported in literature as well as those observed in physiological conditions (*vide supra*).[15]

In conclusion, both the *in-vitro* and *in-vivo* assessment, illustrated that the viability and metabolic activity of the ASCs, as well as the health of the mice, were not affected by the volumetrically 3D-printed constructs. Additionally, no differences were observed between the cross-linked and thermoplastic PCL, which is considered non-toxic and fully biocompatible.[15]

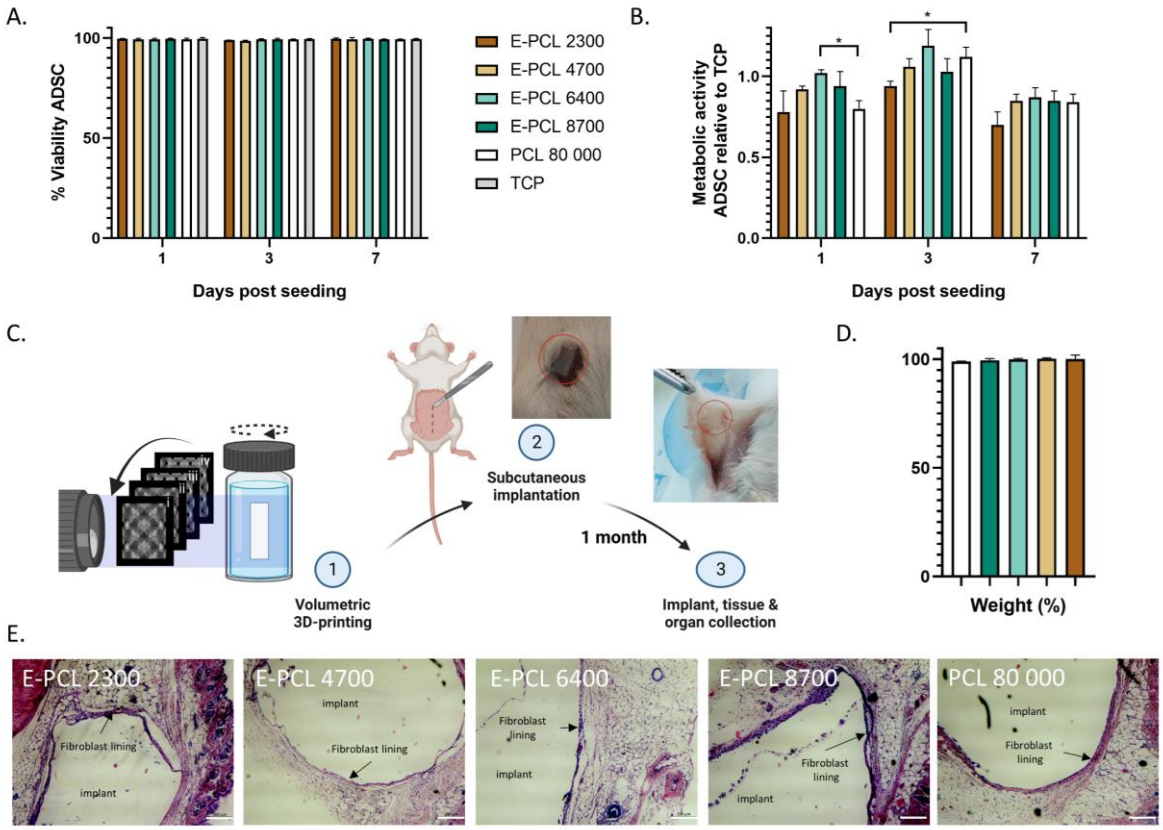

Figure 6. A. Viability (%) of the ASCs after 1, 3 and 7 days of direct contact with the 3D-printed constructs; B. Metabolic activity of the ASCs relative to TCP, as determined via MTS assays, after 1,3 and 7 days of direct contact with the 3D-printed constructs; C. Schematic depiction of the operative procedure during which volumetrically 3D-printed constructs were subcutaneously implanted in immune competent BALB/c mice for a duration of one month; D. Weight loss of the 3D-printed constructs after an implantation period of 1 month illustrating minimal degradation; E. Histopathological evaluation of the tissue surrounding the implants illustrating the presence of a minor foreign body response and limited immune cell infiltration. Scale bar 200 µm.

3. Conclusions and future perspectives

In this work, we introduce photo-cross-linkable PCL networks through orthogonal thiol-ene chemistry. The step-growth polymerized networks are tunable, predictable by means of the rubber elasticity theory and it is shown that their mechanical properties are significantly improved over their acrylate cross-linked counterparts. Tunability is introduced to the materials,

by altering M_c (or the molar mass between cross-links), and its effect on the thermal properties, mechanical strength, degradability and volumetric printability of the materials is evaluated. Moreover, a novel concept is presented for the first time, by which loosely cross-linked materials can be processed into porous designs that would otherwise collapse. Finally, by means of *in-vitro* and *in-vivo* characterization of 3D-printed constructs, we illustrate that the materials can be processed via volumetric printing into biocompatible and non-toxic constructs.

To summarize, this is the first time that volumetric 3D-printing of biodegradable polyesters is reported and we have illustrated the highest resolution for thiol-ene cross-linked systems, to date. The herein introduced materials can be considered promising candidates to serve biomedical applications due to their excellent mechanical properties, tunability, biocompatibility and volumetric 3D-printability.

4. Experimental section

Materials: All chemicals were used as received, unless stated otherwise. ε-caprolactone (>99%), supplied by Tokyo Chemical Industry (TCI), was dried over calcium hydride (CaH_2) and vacuum distilled (120°C, 10 mbar). Allyl isocyanate (98%), ethylene glycol (anhydrous, 99.8%), pentaerythritol (99%), tin(II) 2-ethylhexanoate (92.5-100%), dimethyl terephthalate (99.93%), pentaerythritol tetrakis(3- mercaptopropionate) (>95%) and NaOH (>97%) were supplied by Sigma-Aldrich (Diegem, Belgium). Ethyl(2,4,6-trimethylbenzoyl) phenyl phosphinate (Speedcure TPO-L, 94.5%) was supplied by Lambson Ltd HQ (West Yorkshire, UK). Toluene (>99%), chloroform (stabilised with amylene, >99%) and diethylether (stabilised with 5-7 ppm BHT, >99%) were supplied by Chem-lab NV (Zedelgem, Belgium). Toluene was distilled over sodium with benzophenone as indicator and subsequently stored on molecular sieves (4Å). Deuterated chloroform (stabilised with silver foils + 0.03% TMS, 99.8%) was supplied by Eurisotop.

Synthesis of alkene-functionalized PCL oligomers with varying M_n: The synthesis of telechelic alkene-functionalized PCL (E-PCL) was identical for all PCL precursors. However, in order to

obtain the targeted molar mass, the initiator to monomer ratio was adjusted accordingly. Poly-ε-caprolactone diol with a molar mass of 2300 g/mol was synthesized using the following procedure (molar initiator to monomer ratio of 1:17). A Schlenk equipped with a magnetic stirrer was flame-dried and ε-caprolactone (20 g, 0.175 mol, 1 eq, M = 114.14 $g.mol^{-1}$), $Sn(Oct)_2$ (0.1 g, 0.247 mmol 0.5wt% of ε-caprolactone, 405.122 $g.mol^{-1}$), ethylene glycol (0.639 g, 0.0103 mol, 1:17 stoichiometric ratio initiator to monomer, 62.07$g.mol^{-1}$) and anhydrous toluene (23.75 mL, 4 $mol.L^{-1}$, 92.14 $g.mol^{-1}$) were added under argon atmosphere. Subsequently, three freeze-pump-thaw cycles were performed after which the reaction was left to react for 24 h at 100°C. The reaction was stopped when full conversion was verified by ^{1}H-NMR spectroscopy. Subsequently, the obtained PCL diol was further modified to alkene-functionalized PCL (E-PCL). 1.2 eq. allyl isocyanate (1.55 g, 9.35 mmol, 2 eq., MM = 82.09 $g.mol^{-1}$) was added according to the hydroxyl functionalities and the solution was left to stir for an additional 1h, at 60°C. The reaction was stopped upon full conversion as verified via ^{1}H-NMR spectroscopy. Ultimately, the final product was obtained as a white solid after precipitation in cold diethyl ether.

Synthesis of acrylate-functionalized PCL oligomers with varying M_n: For the synthesis of acrylate-functionalized PCL (A-PCL), PCL diol was first synthesized according to the same procedure shown above. When full conversion was confirmed by ^{1}H-NMR spectroscopy, acryloyl chloride (2 eq., 90.51 $g.mol^{-1}$) and triethyl amine (2 eq., 101.2 $g.mol^{-1}$) were added to the reaction mixture. The reaction was left to proceed until full conversion was verified by ^{1}H-NMR spectroscopy. The final product was then filtered and obtained as a white powder after precipitation in cold diethyl ether.

Determination of the number average molar mass (M_n), alkene content and degree of substitution (DS) via ^{1}H-NMR spectropscopy. The respective PCL oligomer (10 mg) was dissolved in deuterated chloroform and a ^{1}H-NMR spectrum was recorded. NMR spectra were analyzed in Mestrenova and the fully automated baseline correction (Whittacker Smoother) was

applied. The integration of the initiator's methylene moiety (4.2 ppm) was set to 2 and M_n was subsequently determined via the initiator to monomer ratio, using the following formula:

$$M_n\ (g.mol^{-1}) = I_{CL}(\delta 4) * 114.14\ g.mol^{-1} + 2 * 83.09\ g.mol^{-1} + 62.07\ g.mol^{-1} \quad (2)$$

The measurements were performed in triplicate to gain insight into the precision (Table S1). The obtained results are reported as average ± standard deviation. To determine the alkene content, dimethyl terephthalate (DMT, 10 mg, 0.05 mmol, 1 eq., M = 194.18 g.mol^{-1}) was added as internal ^{1}H-NMR standard to 10 mg of the respective PCL precursor and $CDCl_3$. NMR spectra were analyzed in MestReNova software and the fully automatic baseline correction (Whittaker Smoother) was applied. The alkene content was calculated as follows:

$$Alkene\ content\ (mol.g^{-1}) = \frac{I(\delta 5.2)+I(\delta 5.8)}{I(\delta 8)} * \frac{N(DMT)}{N(alkene)} * \frac{m(DMT)}{MM(DMT)} * \frac{1}{m(EUP-PCL)} \quad (3)$$

'I' stands for the integrated value of the peaks compared to the signal from DMT at 8 ppm. 'N' is the amount of protons of DMT and the alkene/acrylate functional group. 'm' refers to the weighed mass and 'MM' refers to the molar mass. The measurements were performed in triplicate to gain insight in the precision (Table S2). The obtained results are reported as average ± standard deviation. The degree of substitution (DS) was determined as the ratio of $M_{n,initiator:CL}$ (calculated according to the initiator to caprolactone ratio by means of equation 2) to $M_{n,DS100}$ (calculated according to the alkene content by assuming DS to be 100%):

$$DS\ (\%) = \frac{M_{n,initiator:CL}}{M_{n,DS100}} * 100 \quad (4)$$

Photo-curing. Alkene-functionalized PCL, PETA-4SH (added according to 1:1 thiol:ene ratio) and TPO-L (0.25wt.% according to PCL precursor) were dissolved in chloroform to ensure proper mixing of all components. The mixture was sonicated and vortexed until fully dissolved. Chloroform was removed upon rotary evaporation and the remaining viscous liquid was placed in a silicone spacer that was positioned between two glass plates, and irradiated with UV-A light (365 nm, 5 mW.cm^{-2}, 30 minutes). As a result, visually homogeneous photo-crosslinked films were obtained. The cross-linked films were dried overnight under vacuum at 40°C. The

light intensity was measured using the RM-12 Radiometer from Opsytec equipped with an UVA sensor. The irradiation set-up was equipped with four light-bulbs (350 blacklight Sylvania).

Characterization: ^{1}H-NMR and ^{13}C-NMR spectroscopy were performed using a Bruker Avance 400 MHz NMR Spectrometer. 16 scans were recorded with a relaxation delay of 1 second and a spectral width of 20 ppm. For quantitative ^{1}H-NMR spectroscopy using DMT as internal standard, the relaxation delay was set at 10 seconds. High resolution magic angle spinning NMR (HR-MAS NMR) spectra were recorded on a Bruker Ultrashield+ 700.13MHz Avance II spectrometer equipped with a 4 mm 1H/13C/119Sn triple channel HR-MAS probe head, equipped with Z-gradients and running Topspin 3.2. Deuterated chloroform was used as solvent. For each measurement, the spinning frequency was set to 6000 Hz, and all measurements were performed at room temperature (25°C). For the ^{1}H experiments, the spectral width used was 20.6 ppm with 32 scans of 64K data points each being accumulated, preceded by 2 dummy scans and a relaxation delay of 30s. Finally, the spectrometer excitation frequency (O1) was set to 4900.91 ppm. Processing consisted of one order of zero filling to 65K real data points, followed by exponential apodisation using a 0.3 Hz line broadening factor prior to Fourier transformation. GPC was performed using a Waters 2695 Alliance Separation Module combined with a RI detector (Waters 2414). GPC measurements were performed at room temperature and 3 PSS SDV (styrene divinylbenzene) GPC columns (particle size 5 µm) with increasing pore size of 1 000, 100 000 and 1 000 000 Å were used. The apparatus was calibrated using polystyrene standards (580 - 1 930 000 g.mol^{-1}) and solutions of 5 mg E-PCL in 1 mL chloroform (HPLC grade) were employed. FTIR spectra were recorded at room temperature on a PerkinElmer Frontier FTIR spectrometer combined with a MK2 golden gate set-up equipped with a diamond crystal from Specac. The spectra were recorded in the range of 600 – 4700 cm^{-1} at a resolution of 4 cm^{-1} and eight scans were accumulated. Gel fraction and swelling properties were determined on discs (4 mm diameter, 0.5 mm thickness) which were

punched out of 2D crosslinked films and immersed during four days in an excess of chloroform. The initial dry mass of the discs (W_d) and the mass of the discs (4 mm diameter) when swollen (W_s) and dried after swelling (W_f) were measured. Using equations (5) and (6), the gel fraction and swelling ratio were calculated, respectively. All measurements were performed in triplicate.

$$Gel\ fraction\ (\%) = \frac{W_f}{W_d}\ x\ 100 \quad (5)$$

$$Swelling\ ratio\ (\%) = \frac{W_s - W_f}{W_f}\ x\ 100 \quad (6)$$

DPC thermograms were recorded with a heat-flux DSC (Mettler DSC823e) coupled to a UV-light source (Hamamatsu Lightningcure LC8) using optical light guides in quartz. The light source was a polychromatic medium pressure mercury–xenon lamp. The irradiance level of 15 mW cm^{-2} was measured with a UVA power meter (Hamamatsu C6080-03 calibrated at 365 nm) at the position of the sample crucible. The experiments were conducted at 20 °C. The temperature and heat flow signal of the DSC cell (Mettler, FRS5) were calibrated using indium. With empty crucibles, the heat flow signal generated by the incident light was largely canceled upon simultaneous illumination of the reference and sample side of the cell. However, imperfect compensation still led to a shift of the baseline upon exposure to the light source. All measurements were conducted using dry nitrogen as inert flow gas (50 ml min^{-1}). Photo-rheology was performed using an Anton Paar Physica MCR 301 rheometer equipped with a UV light-source (365 nm, 10 mW cm^{-2}) with a parallel plate set-up (top plate diameter: 25 mm). Measurements were performed in triplicate. 150 µL of the mixture (E-PCL, PETA-4SH and TPO-L) was placed between the parallel plates and the gap was set to 150 µm. The measurements were performed at 60 °C, at a strain amplitude of 0.1% and an oscillation frequency of 1 Hz. UV-A light was turned on after 15 seconds. Thermogravimetric analyses (TGA) were performed starting from 30 °C up to 600 °C at a heating rate of 10°C.min^{-1}. The degradation temperature was determined at a weight loss of 2 wt.% and a sample mass of 10 mg was used. The analyses were performed on a TGA Q50 (TA instruments). Samples were

measured in a platinum pan under a nitrogen flow of 60 ml.min^{-1}. DSC measurements were performed using a DSC Q2300 (TA Instruments) and a RSC 500 cooler (Zellik, Belgium) employing 5 mg of cross-linked sample. A heating and cooling rate of 10°C per minute was used. The second heating and first cooling ramp are reported in the discussion related to the thermal properties, while the first heating ramp is reported in the discussion related to the mechanical properties. Each sample was measured in an aluminum Tzero pan under nitrogen flow and an empty pan was used as reference. The Q series software was used to analyze the DSC thermograms. Crystallinity was calculated based on an enthalpy of fusion of 136.5 J.g^{-1}.[56] It should be noted that this enthalpy of fusion is based on pure PCL crystals. Due to the presence of the cross-links in between the PCL segments, a slight deviation from these values could be expected. Tensile experiments were performed using a Tinius Olsen Model 1 ST apparatus, equipped with a load cell of 500 N using Horizon as software. Dog bones (gage length 20 mm, thickness 0.5 mm and width 4 mm) were punched out from cross-linked films. The cross-linked films were obtained according to the procedure described above. Measurements were performed in triplicate. An initial strain rate of 1 mm min^{-1} was used up to a force of 0.1 N after which the strain rate was increased to 10 mm min^{-1}. Accelerated (5M NaOH, 37°C) and physiological (PBS, 37°C) degradation assays were performed using 4 and 6 mm diameter discs (thickness of 0.5 mm), respectively. Measurements were performed in triplicate. At each time point, a disc was taken out of the solution, rinsed with water, dried with paper and weighed in order to determine the remaining mass. SEM images of the 3D-printed constructs were captured without application of a coating, using a Hitachi TM-4000 with an accelerating voltage of 15 000 V and a magnification of 35.

Volumetric 3D-printing (VP): VP was performed using a custom printer set-up. For in-depth information regarding the setup, one is referred to the following work.[5] Resins were prepared in the following way. E-PCL was weighed in a vial to which the corresponding amount of PETA-4SH was added. Subsequently, the respective amounts of chloroform, TPO-L (from a

stock solution of 20 mg.mL^{-1} in chloroform) and TEMPO (from a stock solution of 2 mg.mL^{-1} in chloroform) were added. Several cycles of sonication and heating were applied to the resulting mixture, until everything was dissolved. Printing was performed within several minutes of resin preparation. The post-processing procedure was depending on the construct design and material type to be developed. The different post-processing procedures are graphically represented in the supporting information (Figure S17-S19). The first procedure was used for all constructs based on E-PCL 2300, as well as for the tubular constructs used in the printability study and bars used for biological evaluation (Figure S17). The second procedure was used for the development of porous diamond lattices based on E-PCL 4300 (Figure S18). Finally, the third procedure was used for the development of porous diamond lattices based on E-PCL 6400 and E-PCL 8700 (Figure S19). Post-curing was performed using Formlabs Form Cure (375-405 nm, 70 W). For more information regarding the optimization of the projections, resin compositions and respective intensities, one is referred to the supporting information (Figure S30-S35).

In-vitro biocompatibility: Dulbecco's Modified Eagle Medium (DMEM) supplemented with 1 (v/v)% penicillin/streptomycin and 10 (v/v)% fetal bovine serum (FBS) was used to culture adipose-derived Stem Cells (ASC, Lonza) at 37°C in 5% CO2. The culture media was changed twice a week and subculturing followed after reaching 80-90% confluency up to a passage number of 5. A 70 (v/v)% ethanol solution was used to sterilize printed samples for cell culture through incubation for 24 hours with a refreshment step after 12 hours. Afterwards, UV-C irradiation (100-280 nm, 20 mW/cm2 from both sides) was applied for 30 minutes. 10 000 ASC were seeded into the wells of a 96 well plate to initiate the direct contact biocompatibility assay. Volumetrically 3D-printed bars were processed into 3 mm discs with a thickness of approximately 500 µm. After one day, the sterilized samples were placed in direct contact on top of the cultured monolayer. The metabolic activity and viability of the monolayer were investigated through a 3-(4,5-dimethylthiazol-2-yl)-5-(3-carboxymethoxyphenyl)-2-(4-

sulfophenyl)-2H-tetrazolium (MTS) and Live/Dead (Calcein-acetoxymethyl (CA-AM) /Propidium iodide (PI)) assay respectively after one, three and seven days. After removal of the printed samples and the culture medium, a 17 (v/v)% MTS in culture medium was added to the monolayer of cells and incubated in the dark at 37°C for 1 hour after which the absorbance was quantified at 490 nm with a spectrophotometer (Tecan Infinite M200 Pro) to quantify the cell metabolic activity. Moreover, a 2 (v/v)% CA-AM/PI in phosphate buffered saline (PBS) solution was added to the monolayer of cells and incubated in the dark at room temperature for 10 minutes to quantify the cell viability. The cells were visualized through a green fluorescent protein (GFP) and a Texas Red (TxRed) filter of a fluorescence confocal laser scanning microscope (Carl Zeiss LSM 710). The percentage viability was computed through the use of FIJI software.

In-vivo biocompatibility: This study was approved by the Animal Ethical Committee of the Faculty of Medicine and Health Sciences at Ghent University, Belgium (DEC 19-08). Female BALB/c mice 6-8 weeks old, were purchased from Charles River Laboratories, France. All investigators in the study are Category C Animal Experiment Leader certified by the Federation of European Laboratory Animal Science Association. All efforts were made to minimize animal suffering. Animals were housed on a 12–12 light cycle (light on 6am, off 6pm) and were provided food and water ad libitum. Animals were anesthetized with Sevoflurane (induction 8%, maintenance 4.5 – 3.5%, flow 0.8-1L/min). A small incision in the skin was made using surgical scissors on the lower abdominal region and a small pocket was created medially from the incision right under the skin by blunt dissection. A 3D-printed implant of 5 x 3 x 2 mm^3 was then placed in the pocket and the incision was closed with sutures. In every group, four mice were operated and two implants were inserted, one at each side. The control group underwent the same procedure, but no implant was placed in the pocket. The mice's behavior and weight were observed during the study, and 4 weeks post-implantation, the mice were euthanized and a necropsy was performed. The weight of the spleen was determined, as an enlarged spleen is

a sign of inflammation. Lever, kidney and spleen were collected for histopathological evaluation with Haematoxylin and Eosin (H&E) staining. One implant per mouse was extracted and used to evaluate degradation, after removal of the surrounding tissue. The other implant was fixated together with the surrounding tissue for histopathological evaluation. Organs and implants were fixated in 4% paraformaldehyde and immersed in increasing concentrations of alcohol to dehydrate the tissues prior to paraffin embedding. Xylene and Ultraclear (J.T. Baker) were used as clearing agent for organ and implants respectively. Sections were stained using a standard H&E and immunohistochemistry protocol applied in clinical pathology. During the embedding and staining procedure, the implant is dissolved while the surrounding tissue remains.[57]

Supporting Information

Supporting Information is available from the Wiley Online Library or from the author.

Acknowledgements

The authors would like to acknowledge funding from FWO (FWO-SB fellow - 1SA2321N). Furthermore, the authors would also like to acknowledge FWO for the provided travel grant to support a research stay at the University of California, Berkeley. J.T.T. and H.K.T. were supported by funded by the National Science Foundation under cooperative agreement no. EEC-1160494. The 700 MHz used in this work is part of the NMR Expertise Centre at UGent and was funded through an FFEU-ZWAP grant awarded to Prof. J. Martins (UGent).

Received: ((will be filled in by the editorial staff))

Revised: ((will be filled in by the editorial staff))

Published online: ((will be filled in by the editorial staff))

References

[1] M. Jafari, Z. Paknejad, M. R. Rad, S. R. Motamedian, M. J. Eghbal, N. Nadjmi, A.

Khojasteh, *J. Biomed. Mater. Res. Part B* **2017**, *105*, 431.

[2] P. Tack, J. Victor, P. Gemmel, L. Annemans, *Biomed. Eng. Online* **2016**, *15*, 1.

[3] N. Martelli, C. Serrano, H. Van Den Brink, J. Pineau, P. Prognon, I. Borget, S. El Batti, *Surg. (United States)* **2016**, *159*, 1485.

[4] B. E. Kelly, I. Bhattacharya, H. Heidari, M. Shusteff, C. M. Spadaccini, H. K. Taylor, *Science (80-.).* **2019**, *363*, 1075.

[5] J. T. Toombs, M. Luitz, C. C. Cook, S. Jenne, C. C. Li, B. E. Rapp, F. Kotz-Helmer, H. K. Taylor, *Science (80-.).* **2022**, *376*, 308.

[6] P. N. Bernal, P. Delrot, D. Loterie, Y. Li, J. Malda, C. Moser, R. Levato, *Adv. Mater.* **2019**, *31*, DOI 10.1002/adma.201904209.

[7] B. Wang, E. Engay, P. R. Stubbe, S. Z. Moghaddam, E. Thormann, K. Almdal, A. Islam, Y. Yang, *Nat. Commun.* **2022**, *13*, DOI 10.1038/s41467-022-28013-4.

[8] R. Rizzo, D. Ruetsche, H. Liu, M. Zenobi-Wong, *Adv. Mater.* **2021**, *33*, 2102900.

[9] L. S. Nair, C. T. Laurencin, *Prog. Polym. Sci.* **2007**, *32*, 762.

[10] Z. Sheikh, S. Najeeb, Z. Khurshid, V. Verma, H. Rashid, M. Glogauer, *Materials* **2015**, *8*, 5744.

[11] D. Ozdil, H. M. Aydin, *J. Chem. Technol. Biotechnol.* **2014**, *89*, 1793.

[12] G. Thrivikraman, A. Athirasala, C. Twohig, S. K. Boda, L. E. Bertassoni, *Dent. Clin. North Am.* **2017**, *61*, 835.

[13] H. E. Jazayeri, M. Tahriri, M. Razavi, K. Khoshroo, F. Fahimipour, E. Dashtimoghadam, L. E. Almeida, L. Tayebi, *Mater. Sci. Eng. C* **2017**, *70*, 913.

[14] T. Ghassemi, A. Shahroodi, M. H. Ebrahimzadeh, A. Mousavian, J. Movaffagh, A. Moradi, *Arch. Bone Jt. Surg.* **2018**, *6*, 90.

[15] M. A. Woodruff, D. W. Hutmacher, *Prog. Polym. Sci.* **2010**, *35*, 1217.

[16] A. Arslan, W. Steiger, P. Roose, H. Van den Bergen, P. Gruber, E. Zerobin, F. Gantner, O. Guillaume, A. Ovsianikov, S. Van Vlierberghe, P. Dubruel, *Mater. Today* **2020**, *44*,

25.

[17] B. J. Green, K. S. Worthington, J. R. Thompson, S. J. Bunn, M. Rethwisch, E. E. Kaalberg, C. Jiao, L. A. Wiley, R. F. Mullins, E. M. Stone, E. H. Sohn, B. A. Tucker, C. A. Guymon, *Biomacromolecules* **2018**, *19*, 3682.

[18] J. R. Thompson, K. S. Worthington, B. J. Green, N. K. Mullin, C. Jiao, E. E. Kaalberg, L. A. Wiley, I. C. Han, S. R. Russell, E. H. Sohn, C. A. Guymon, R. F. Mullins, E. M. Stone, B. A. Tucker, *Acta Biomater.* **2019**, *94*, 204.

[19] P. Yang, G. Zhu, S. Xu, X. Zhang, X. Shen, X. Cui, Y. Gao, J. Nie, *J. Polym. Sci. Part B Polym. Phys.* **2017**, *55*, 692.

[20] J. Wang, J. Li, X. Wang, Q. Cheng, Y. Weng, J. Ren, *React. Funct. Polym.* **2020**, *155*, 104695.

[21] J. J. Tzeng, Y. T. Hsiao, Y. C. Wu, H. Chen, S. Y. Lee, Y. M. Lin, *Biomed Res. Int.* **2018**, *2018*, DOI 10.1155/2018/8719624.

[22] H. Zhu, T. Kimura, S. Swami, J. Y. Wu, *Biomaterials* **2019**, *196*, 31.

[23] Q. Thijssen, L. Parmentier, E. Augustyniak, P. A. Mouthuy, S. Van Vlierberghe, *Adv. Funct. Mater.* **2022**, *32*, 2108869.

[24] Q. Thijssen, K. Cornelis, R. Alkaissy, J. Locs, L. Van Damme, D. Schaubroeck, R. Willaert, S. Snelling, P.-A. Mouthuy, S. Van Vlierberghe, *Biomacromolecules* **2022**, acs. biomac.1c01584.

[25] A. F. Senyurt, H. Wei, B. Phillips, M. Cole, S. Nazarenko, C. E. Hoyle, S. G. Piland, T. E. Gould, *Macromolecules* **2006**, *39*, 6315.

[26] H. J. Yoo, Y. H. Lee, J. Y. Kwoit, H. Do Kim, *Fibers Polym.* **2001**, *2*, 122.

[27] T. Kuhnt, F. L. C. Morgan, M. B. Baker, L. Moroni, *Addit. Manuf.* **2021**, *46*, 102102.

[28] R. Wang, F. Damanik, T. Kuhnt, H. Ippel, P. J. Dijkstra, A. Tessa ten Cate, A. Dias, L. Moroni, M. B. Baker, R. Wang, F. Damanik, T. Kuhnt, P. Dijkstra, L. Moroni, M. Baker, H. Ippel, A. Dias, *ChemRxiv* **2020**, DOI 10.26434/CHEMRXIV.12053037.V1.

[29] M. Baker, R. Wang, F. Damanik, T. Kuhnt, H. Ippel, P. Dijkstra, T. Cate, A. Dias, L. Moroni, **2020**, DOI 10.26434/chemrxiv.12053037.v1.

[30] K. S. Lee, D. S. Kim, B. S. Kim, *Biotechnol. Bioprocess Eng.* **2007**, *12*, 152.

[31] L. Cai, S. Wang, *Polymer* **2010**, *51*, 164.

[32] H. Y. Kweon, M. K. Yoo, I. K. Park, T. H. Kim, H. C. Lee, H. S. Lee, J. S. Oh, T. Akaike, C. S. Cho, *Biomaterials* **2003**, *24*, 801.

[33] E. Lin, Z. Wang, X. Zhao, Z. Liu, D. Yan, F. Jin, Y. Chen, P. Cheng, Z. Zhang, *Angew. Chemie - Int. Ed.* **2022**, *61*, DOI 10.1002/ANIE.202117390.

[34] N. R. Richbourg, M. Wancura, A. E. Gilchrist, S. Toubbeh, B. A. C. Harley, E. Cosgriff-Hernandez, N. A. Peppas, *Sci. Adv.* **2021**, *7*, 3245.

[35] B. H. Northrop, R. N. Co, *J. Am. Chem. Soc.* **2012**, 13804.

[36] A. F. Senyurt, H. Wei, C. E. Hoyle, S. G. Piland, T. E. Gould, *Macromolecules* **2007**, *40*, 4901.

[37] S. E. Kasprzak, B. A. Wester, T. Raj, M. Allen, K. Gall, *J. Microelectromechanical Syst.* **2013**, *22*, 339.

[38] N. B. Cramer, C. N. Bowman, *J. Polym. Sci. Part A Polym. Chem.* **2001**, *39*, 3311.

[39] N. B. Cramer, S. K. Reddy, A. K. O'Brien, C. N. Bowman, *Macromolecules* **2003**, *36*, 7964.

[40] S. S. Sheiko, A. V. Dobrynin, *Macromolecules* **2019**, *52*, 7531.

[41] L. H. Sperling, *Introd. to Phys. Polym. Sci.* **2005**, 239.

[42] L. S. Nair, C. T. Laurencin, *Prog. Polym. Sci.* **2007**, *32*, 762.

[43] S. Yang, K. F. Leong, Z. Du, C. K. Chua, *https://home.liebertpub.com/ten* **2004**, *7*, 679.

[44] L. Fambri, A. Penati, J. Kolarik, *Die Angew. Makromol. Chemie* **1995**, *228*, 201.

[45] R. G. Schoenmakers, P. Van De Wetering, D. L. Elbert, J. A. Hubbell, *J. Control. Release* **2004**, *95*, 291.

[46] L. H. Sperling, *Introd. to Phys. Polym. Sci.* **2005**, 557.

[47] L. H. Sperling, *Introd. to Phys. Polym. Sci.* **2005**, 427.

[48] M. Maroulakos, G. Kamperos, L. Tayebi, D. Halazonetis, Y. Ren, *J. Dent.* **2019**, *80*, 1.

[49] C. C. Cook, E. J. Fong, J. J. Schwartz, D. H. Porcincula, A. C. Kaczmarek, J. S. Oakdale, B. D. Moran, K. M. Champley, C. M. Rackson, A. Muralidharan, R. R. McLeod, M. Shusteff, C. C. Cook, E. J. Fong, J. J. Schwartz, D. H. Porcincula, A. C. Kaczmarek, J. S. Oakdale, B. D. Moran, K. M. Champley, M. Shusteff, C. M. Rackson, R. R. McLeod, A. Muralidharan, *Adv. Mater.* **2020**, *32*, 2003376.

[50] C. C. Cook, E. J. Fong, J. J. Schwartz, D. H. Porcincula, A. C. Kaczmarek, J. S. Oakdale, B. D. Moran, K. M. Champley, C. M. Rackson, A. Muralidharan, R. R. McLeod, M. Shusteff, *Adv. Mater.* **2020**, *32*, 1.

[51] K. Phillipson, M. J. Jenkins, J. N. Hay, *J. Therm. Anal. Calorim.* **2016**, *123*, 1491.

[52] K. Phillipson, M. J. Jenkins, J. N. Hay, *Eur. Polym. J.* **2016**, *84*, 708.

[53] W. P. Paré, G. B. Glavin, *Neurosci. Biobehav. Rev.* **1986**, *10*, 339.

[54] M. Kraiger, T. Klein-Rodewald, B. Rathkolb, J. Calzada-Wack, A. Sanz-Moreno, H. Fuchs, E. Wolf, V. Gailus-Durner, M. H. de Angelis, *Sci. Reports 2022 121* **2022**, *12*, 1.

[55] E. Dondossola, B. M. Holzapfel, S. Alexander, S. Filippini, D. W. Hutmacher, P. Friedl, *Nat. Biomed. Eng. 2016 11* **2016**, *1*, 1.

[56] P. Yang, G. Zhu, S. Xu, X. Zhang, X. Shen, X. Cui, Y. Gao, J. Nie, *J. Polym. Sci. Part B Polym. Phys.* **2017**, *55*, 692.

[57] A. T. Feldman, D. Wolfe, *Methods Mol. Biol.* **2014**, *1180*, 31.

Thiol-ene cross-linkable PCL is introduced and the effect of the cross-link density on the networks' physico-chemical properties, volumetric printability and biocompatibility is investigated. Notably, this is the first report on volumetric 3D-printing of polyesters and we illustrate 3D-printing of the smallest features to date, for non-acrylate-based resins.

Q. Thijssen, A. Quaak, J. Toombs, E. De Vlieghere, L. Parmentier, H. Taylor, S. Van Vlierberghe

Volumetric Printing of Thiol-Ene Photo-Cross-Linkable PCL: A Tunable Material Platform serving Biomedical Applications